JACS
JOURNAL OF THE AMERICAN CHEMICAL SOCIETY

pubs.acs.org/JACS

Article

Densified HKUST-1 Monoliths as a Route to High Volumetric and Gravimetric Hydrogen Storage Capacity

David Gerard Madden,*[,|||] Daniel O'Nolan,[|||] Nakul Rampal,[|||] Robin Babu, Ceren Çamur, Ali N. Al Shakhs, Shi-Yuan Zhang, Graham A. Rance, Javier Perez, Nicola Pietro Maria Casati, Carlos Cuadrado-Collados, Denis O'Sullivan, Nicholas P. Rice, Thomas Gennett, Philip Parilla, Sarah Shulda, Katherine E. Hurst, Vitalie Stavila, Mark D. Allendorf, Joaquin Silvestre-Albero, Alexander C. Forse, Neil R. Champness, Karena W. Chapman,* and David Fairen-Jimenez*

Cite This: *J. Am. Chem. Soc.* 2022, 144, 13729−13739

Read Online

ACCESS | Metrics & More | Article Recommendations | Supporting Information

ABSTRACT: We are currently witnessing the dawn of hydrogen (H_2) economy, where H_2 will soon become a primary fuel for heating, transportation, and long-distance and long-term energy storage. Among diverse possibilities, H_2 can be stored as a pressurized gas, a cryogenic liquid, or a solid fuel *via* adsorption onto porous materials. Metal−organic frameworks (MOFs) have emerged as adsorbent materials with the highest theoretical H_2 storage densities on both a volumetric and gravimetric basis. However, a critical bottleneck for the use of H_2 as a transportation fuel has been the lack of densification methods capable of shaping MOFs into practical formulations while maintaining their adsorptive performance. Here, we report a high-throughput screening and deep analysis of a database of MOFs to find optimal materials, followed by the synthesis, characterization, and performance evaluation of an optimal monolithic MOF ($_{mono}$MOF) for H_2 storage. After densification, this $_{mono}$MOF stores 46 g L^{-1} H_2 at 50 bar and 77 K and delivers 41 and 42 g L^{-1} H_2 at operating pressures of 25 and 50 bar, respectively, when deployed in a combined temperature−pressure (25−50 bar/77 K → 5 bar/160 K) swing gas delivery system. This performance represents up to an 80% reduction in the operating pressure requirements for delivering H_2 gas when compared with benchmark materials and an 83% reduction compared to compressed H_2 gas. Our findings represent a substantial step forward in the application of high-density materials for volumetric H_2 storage applications.

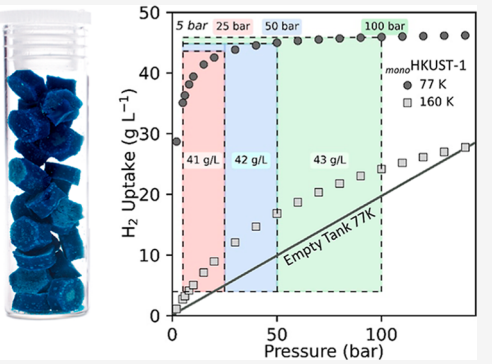

INTRODUCTION

We are currently living in a time of great change as global transport transitions away from fossil fuels. As an alternative, H_2 gas has long held great promise as a sustainable energy vector and an automotive transportation fuel as part of the H_2 economy.[1−3] H_2 gas is a clean, potentially green, and non-toxic renewable fuel that contains much greater chemical energy per mass (142 MJ kg^{-1}) when compared to hydrocarbon fuels. The combustion of H_2 releases only water vapor as a by-product, allowing H_2 fuel cell vehicles (FCV) to potentially provide zero-emission transportation. While containing *ca.* three times more energy per unit mass than gasoline, its onboard storage presents significant challenges. H_2 is a very light gas and displays weak $H_2\cdots H_2$ intermolecular forces, thus requiring cryogenic cooling and/or compression for storage at quantities (>5.6 kg) deemed sufficient for driving ranges (*ca.* 300 miles) comparable to traditional fuels.[4]

The US Department of Energy (DOE) set ambitious targets for FCV onboard H_2 storage, requiring an initial system (including tank and materials) delivery capacity of 30 g L^{-1} (4.5 wt %) and an ultimate target of 50 g L^{-1} (6.5 wt %). FCVs utilizing compressed H_2 gas (CHG) and cryo-compression methods have already been produced by major automobile manufacturers (BMW, Toyota, and Honda). However, these vehicles still require high gas operating pressures (>350 bar) and costly carbon fiber-reinforced storage tanks. Adsorbed gas storage (AGS) is considered a viable alternative to cryogenic or compressive storage, utilizing nanoporous materials to boost the hydrogen density in a tank at reduced operating pressures (*ca.* 100 bar). While traditional nanoporous materials such as activated carbons have been widely studied for H_2 storage, these materials lack the versatility and structural tunability to be considered viable options for AGS technologies.[5−7]

Received: April 30, 2022
Published: July 25, 2022

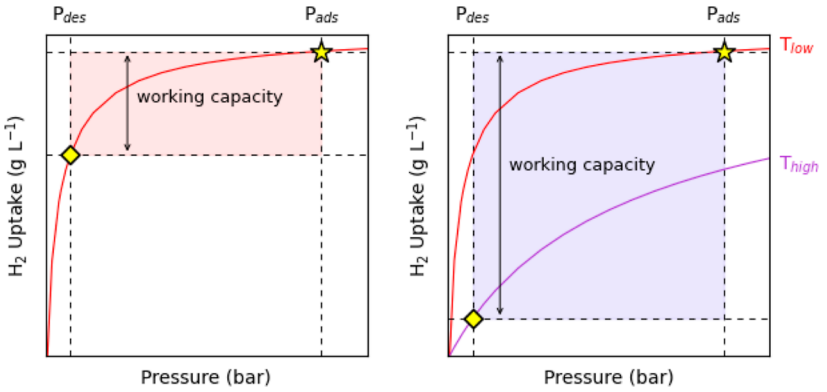

Figure 1. Idealized H_2 adsorption isotherms for FCV storage systems. Illustration of usable volumetric capacity for (a) pressure swing and (b) temperature−pressure swing storage systems. Total volumetric adsorption isotherms are shown as purple and red curves, corresponding to high and low temperatures, respectively. The "charged" state of the tank is represented by a gold star, and the "discharged" state is represented by gold diamonds. Double-sided arrows represent volumetric usable capacities achieved for each system, with P_{ads} = 100 bar and P_{des} = 5 bar.

As an alternative, metal−organic frameworks (MOFs) are a class of nanoporous materials with a great potential for gas storage and separation applications. The tunability of this class of materials has given way to the synthesis of over 100,000 reported structures with a large array of interesting properties in terms of chemical and structural diversity.[8,9] This versatility of MOFs has made them widely studied for AGS applications, including H_2 and CH_4. Several high-surface-area MOFs display benchmark performance with impressive gravimetric and volumetric H_2 storage densities, both on the materials and system-based levels.[4] Despite these advances, two major issues need to be addressed before MOFs can be deployed in FCVs. First, MOFs generally display type I isotherms for the adsorption of H_2 under cryogenic conditions (Figure 1), with very high loadings at low pressures, followed by a saturation of the H_2 uptake at higher pressures. This limits the overall working capacity of the adsorbent materials. To address this issue, the DOE Hydrogen Storage Engineering Center of Excellence (HSECoE) has proposed designing tanks for cryo-adsorption storage that operate with H_2 loading occurring at 77 K and 100 bar and discharge occurring at 160 K and 5 bar, ensuring that the amount of deliverable H_2 in nanoporous MOFs is maximized (Figure 1).[10]

The second, and arguably more important, issue hampering the deployment of MOFs for gas storage applications is the shaping and densification of MOF materials. While many MOFs display exceptional gravimetric H_2 adsorption capacity, their performance does not readily translate to volumetric performance due to issues relating to MOF densification. MOFs are traditionally synthesized as powders with very low packing density that are formulated into shaped bodies *via* mechanical processes.[11−13] These processes often yield low-density final products or materials with reduced performance as a result of the low pressures used in the processing or structural collapse when the pressures are high.[12,14] Despite its importance, this is an area of research that has received relatively low attention, with many researchers choosing to report volumetric values based upon theoretical crystal densities as opposed to experimental bulk densities.[15] While theoretical crystal densities play an important role in identifying candidate materials for H_2 storage, the final packing densities of shaped materials can often be only a fraction of the theoretical crystal densities. Indeed, many MOFs suffer significant losses in porosity and overall adsorption performance upon densification due to pore collapse.[12,16,17] As an alternative to the densification of bulk powders, control of particle size, morphology, and monodispersity before densification has recently shown potential for improving the packing densities for MOFs.[18]

In this work, we first used high-throughput computational screening and principal component analysis (PCA) to evaluate the landscape of the properties required to optimize hydrogen uptake in MOFs and to find an optimal structure, HKUST-1. Then, we used our recent developments in advanced sol−gel synthesis, engineering, and densification of MOFs to produce a pure monolithic HKUST-1 ($_{mono}$HKUST-1) structure of up to about 1 cm^3 in size without using high pressures or additional binders.[17,19−21] We subsequently examined the unique nature of the local structures of the high-density $_{mono}$HKUST-1 material using advanced characterization techniques such as synchrotron X-ray total scattering, mapping pair distribution function (PDF) studies, Raman microscopy, and solid-state nuclear magnetic resonance (NMR) spectroscopy studies. Finally, we examined the exceptional adsorption performance of $_{mono}$HKUST-1 as the top-performing densified MOF for volumetric H_2 storage. The performance of $_{mono}$HKUST-1 suggests that advanced monolithic MOFs could pave the way for a new generation of high-performance, high-density adsorbents for both onboard vehicular AGS and stationary applications, dramatically reducing the pressure requirements for onboard H_2 storage while improving both vehicle safety and driving distances in support of the H_2 economy.

RESULTS AND DISCUSSION

High-Throughput Computational Screening of MOFs.

The exceptional tunability of MOFs has led to the experimental synthesis of thousands of MOFs and the prediction of millions.[8,22] To evaluate the landscape of MOFs in hydrogen storage in this vast chemical space, we conducted high-throughput screening (HTS) studies by performing grand canonical Monte Carlo (GCMC) simulations on a database of 2,932 experimentally synthesized MOFs at four pressures of 5, 25, 50, and 100 bar and five temperature of 77, 160, 198, 233, and 298 K. We went one step further by performing a PCA on the vast amount of data generated in the HTS studies. We also highlighted 10 benchmark MOF materials for hydrogen storage in our screening—HKUST-1, MOF-5, NU-100/PCN-100, NU-

https://doi.org/10.1021/jacs.2c04608
J. Am. Chem. Soc. 2022, 144, 13729−13739

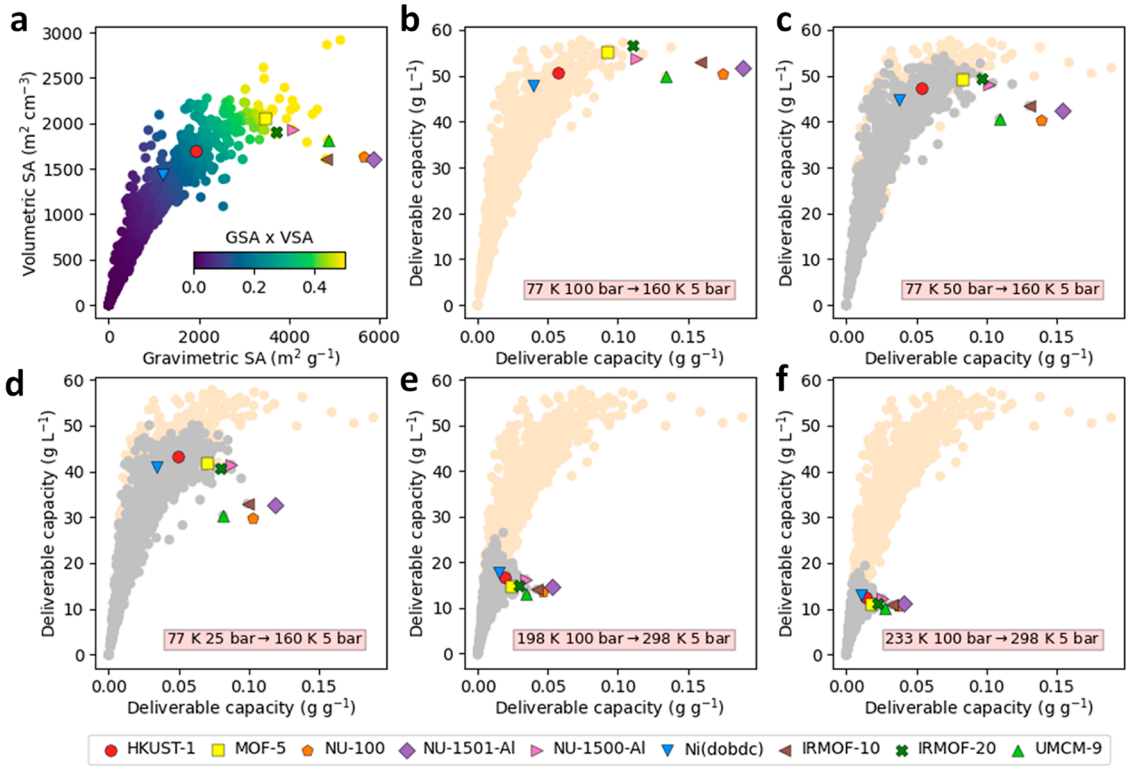

Figure 2. Computational screening of benchmark MOF materials. (a) Relationship between volumetric and gravimetric BET areas for 2940 MOFs. (b) Hydrogen volumetric and gravimetric deliverable capacities for a combined temperature−pressure H_2 delivery system (100 bar/77 K → 5 bar/160 K). (c) Hydrogen volumetric and gravimetric deliverable capacities for a combined temperature−pressure H_2 delivery system (50 bar/77 K → 5 bar/160 K). (d) Hydrogen volumetric and gravimetric deliverable capacities for a combined temperature−pressure H_2 delivery system (25 bar/77 K → 5 bar/160 K). (e) Hydrogen volumetric and gravimetric deliverable capacities for a combined temperature−pressure H_2 delivery system (100 bar/198 K → 5 bar/298 K). (f) Hydrogen volumetric and gravimetric deliverable capacities for a combined temperature−pressure H_2 delivery system (100 bar/233 K → 5 bar/298 K). Peach-colored points in (b) to (f) represent H_2 performance for a 100 bar/77 K → 5 bar/160 K system, while gray points represent H_2 performance for the named system in (c) to (f).

1501-Al, NU-1500-Al, Ni(dobdc), MIL-101, IRMOF-10, UMCM-9, and IRMOF-20. Although some previous HTS studies have been reported in the literature, none have explored the range of conditions considered here.[23−25]

Figure 2a shows the general landscape of the gravimetric and volumetric surface areas of the MOFs studied here. Benchmark MOF materials such as MOF-5, IRMOF-20, and NU-1500-Al displayed both exceptional gravimetric and volumetric surface areas. While materials such as NU-1501-Al and NU-100 displayed high gravimetric surface areas, the denser structure of HKUST-1 gave way to a higher volumetric surface area. On top of that, for hydrogen tank storage, an ideal MOF structure should not only have a high hydrogen storage capacity but, more importantly, should also possess a high deliverable capacity.[15] To further probe the gas storage/adsorption performance, we determined the theoretical H_2 deliverable capacities of the studied MOFs under five different combined temperature−pressure swing gas delivery systems, ranging from purely cryogenic (25, 50, and 100 bar/77 K → 5 bar/160 K) to near-ambient H_2 delivery (100 bar/198 K and 100 bar/233 K → 5 bar/298 K). Figure 2b−f show the gravimetric and volumetric H_2 deliverable capacities; the raw data are available in a dynamic visualization tool at: https://aam.ceb.cam.ac.uk/mofexplorer.html. Part 1 of the tool contains the data for purely cryogenic H_2 delivery, whereas part 2 contains the data for near-ambient H_2 delivery. Under cryogenic conditions and high pressure (100 bar/77 K), benchmark MOFs such as MOF-5, IRMOF-20, NU-1500-Al, IRMOF-10, and NU-1501-Al get the highest values in terms of both gravimetric and volumetric deliverable capacity (Figure 2b). Interestingly, as the storage pressure decreases (Figure 2c,d), denser MOFs with open-metal sites such as HKUST-1 and Ni(dobdc) begin to match and outperform large gravimetric surface area materials under volumetric conditions; the deliverable capacities of H_2 for HKUST-1 display *ca.* 10% reduction when the storage pressure is reduced from 100 to 25 bar at 77 K. Under near-ambient conditions, HKUST-1 and Ni_2(dobdc) outperformed all the other benchmark materials in terms of volumetric deliverable capacity. The exceptional performance of HKUST-1 and Ni_2(dobdc) can be attributed to the denser crystal structure and high density of unsaturated metal centers, which give way to enhanced adsorbate−adsorbent interactions. The results of the HTS suggest that higher surface areas and larger pore volumes give way to exceptional H_2 deliverable capacities at low temperatures and high pressures. Conversely, and as expected, denser structures and stronger adsorbent−adsorbate interactions give way to enhanced H_2 deliverable capacities at lower pressures and higher temperatures.[12,23,26]

Once the HTS data have been collected, we moved to a PCA. Commonly used for dimensionality reduction, PCA helps to choose the minimum number of variables needed to explain the maximum amount of variance in the dataset. The raw data for the PCA are available in the dynamic PCA visualization tool at https://hydrogen-storage-pca.herokuapp.com. The Supporting Information (Figures S8−S10 and Table S7) provides more details about the geometric properties'

https://doi.org/10.1021/jacs.2c04608
J. Am. Chem. Soc. 2022, 144, 13729−13739

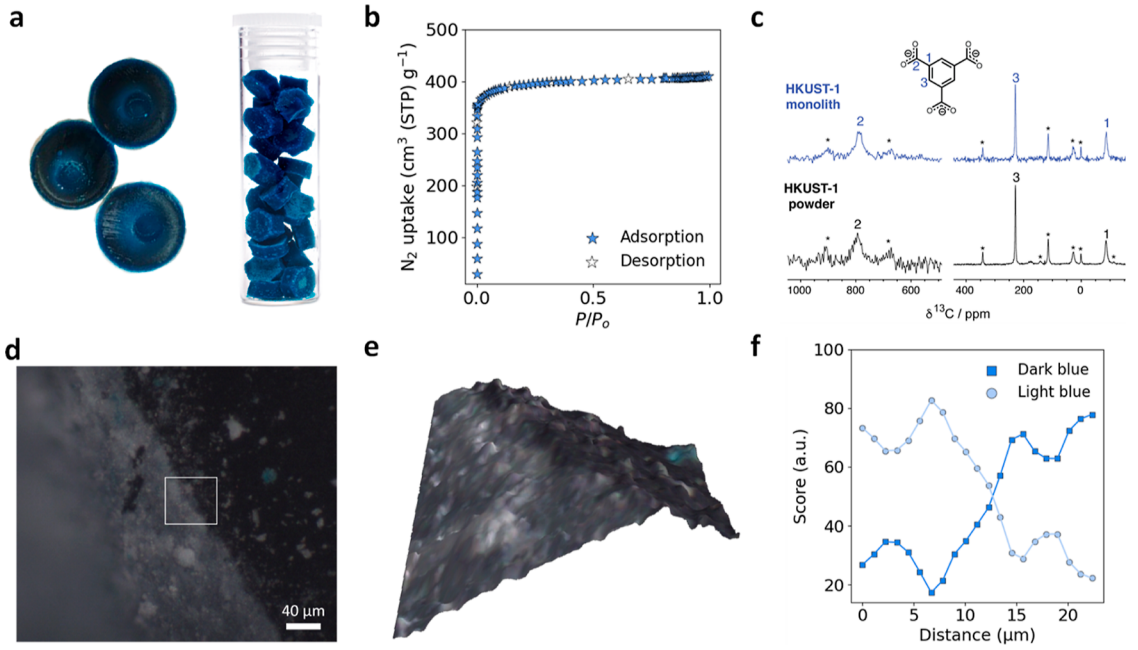

Figure 3. Characterization, NMR spectroscopy, and Raman microscopy studies of pristine $_{mono}$HKUST-1. (a) Optical images of $_{mono}$HKUST-1 prepared via traditional (Left) and scaled-up synthesis (Right). (b) Linear plot of the 77 K N_2 adsorption isotherm for $_{mono}$HKUST-1. (c) ^{13}C NMR spectra of $_{mono}$HKUST-1 and HKUST-1 powder samples. (d) Optical image and (e) three-dimensional reconstruction of the $_{mono}$HKUST-1 section mapped by Raman microscopy, (f) showing the corresponding normalized CLS scores associated with Raman spectra of the dark blue and light blue portions over the mapped section.

calculation, HTS studies, and PCA. From these studies, it is clear that optimizing the density of the material along with selecting an appropriate adsorption pressure for the process is crucial. Indeed, while it is clear that densification is key for the deployment of MOFs,[15] it is also well known that the excess capacity reaches a maximum and then declines with increasing pressure because it becomes more efficient to pack molecules in the gas phase than on the surface.[27]

Synthesis and Characterization. Based on the HTS and PCA, we selected HKUST-1. Not only are its predicted volumetric absolute and deliverable capacities high but also looking at industrial production, it is based on a commercially available organic ligand and a simple synthesis process. In addition to standard synthetic methods, HKUST-1 can be made through spray-drying[28] and mechanosynthesis.[29] Here, we performed the synthesis of HKUST-1 not as a powder but as a high-density $_{mono}$HKUST-1 using the previously reported sol−gel method.[17] After the formation of the crystalline primary MOF particles at the beginning of the reaction, the mother solution was centrifuged, and the resulting MOF gel was washed to remove unreacted precursors. After three washing steps, the MOF gel was then allowed to dry overnight at room temperature, resulting in the formation of $_{mono}$HKUST-1. Figure 3a displays an optical image of $_{mono}$HKUST-1, while Figure S1 displays the powder X-ray diffraction (PXRD) patterns of the material. Once the $_{mono}$HKUST-1 was dry, activation was carried out by heating to 120 °C under vacuum for 12 h. The $_{mono}$HKUST-1 retains the macroscopic monolithic morphology and shape of the mold after activation. We obtained the envelope and particle packing densities of the monolithic and powdered materials, respectively, by mercury intrusion porosimetry (Figure S26). The measured envelope density of $_{mono}$HKUST-1 is in agreement with the previously reported data, with an overall density of 1.07 g cm^{-3}[17] and verified by Particle Authority as a part of NREL H_2 capacity characterization. We then evaluated the porosity using N_2 adsorption at 77 K (Figures 3b, S2, and S3). Table S19 compares the densities, gravimetric and volumetric Brunauer, Emmett, and Teller (BET) areas calculated using Rouquerol's updated criteria implemented in BETSI (Figures S4 and S5),[30] and pore volumes of $_{mono}$HKUST-1 with those of powder and densified benchmark MOF materials. While $_{mono}$HKUST-1 displays one of the lowest observed gravimetric BET areas (1552 m^2 g^{-1}) and total pore volume (0.634 cm^3 g^{-1}) of the materials presented, the critical advantage of the monolithic MOF is the high bulk density, which enables benchmark volumetric performance (BET area = 1,651 m^2 cm^{-3}; pore volume = 0.675 cm^3 cm^{-3}) which far exceeds that of powdered and mechanically pressed MOF counterparts (Table S19 and Figure S46).[12,16,31] The measured bulk density of $_{mono}$HKUST-1 (1.07 g cm^{-3}) is higher than the crystal densities of HKUST-1 (0.883 g cm^{-3}), which can be attributed to the presence of amorphous, denser phases within the monolithic material.[17] Similar observations of high bulk density retention leading to high microporosity have been seen for previously studied $_{mono}$ZIF-8 and $_{mono}$UiO-66.[20,21]

Aiming to see if there are any structural or chemical differences between the powder and monolithic materials, we first examined the local environment of $_{mono}$HKUST-1 by NMR spectroscopy. The ^{13}C NMR spectra (Figure 3c) for $_{mono}$HKUST-1 and HKUST-1 powder show similar peak assignments (Table S18) to those previously reported in the literature for HKUST-1,[32] with no additional local environments observed for the BTC^{3-} linker (BTC^{3-} = 1,3,5-benzenetricarboxylate) in any sample. These results suggest, therefore, that the local chemical environment of the linker molecule in the powder and monolith materials is very similar

https://doi.org/10.1021/jacs.2c04608
J. Am. Chem. Soc. 2022, 144, 13729−13739

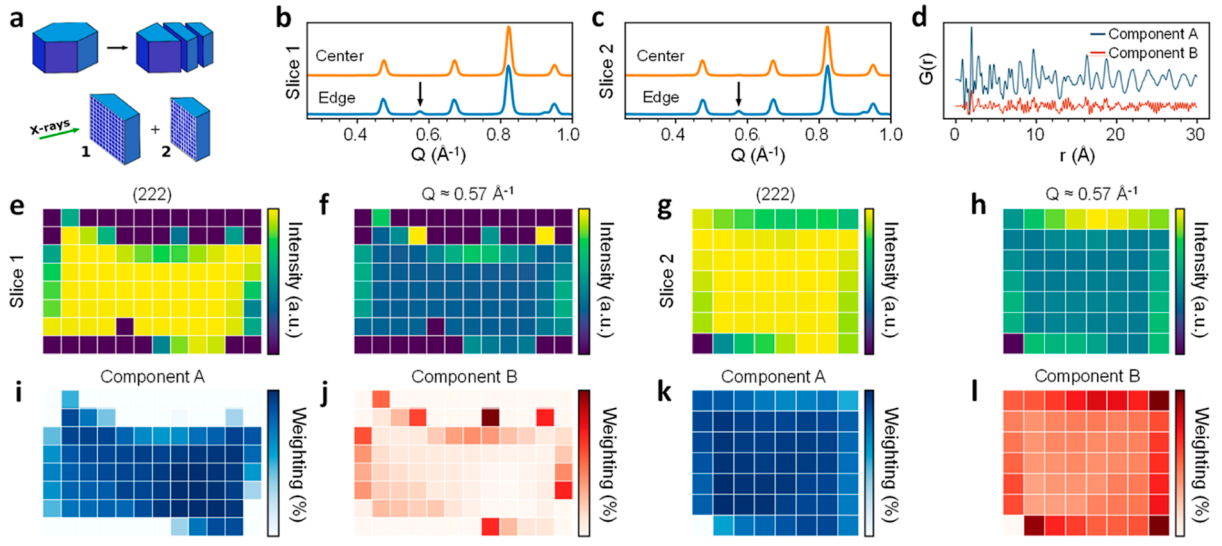

Figure 4. Mapping XRD and PDF studies for $_{mono}$HKUST-1. (a) Monolithic samples were segmented into slices, and X-rays were used to map their cross-sections. (b,c) PXRD patterns collected at the edge (blue) and center (orange) of slices 1 and 2, respectively. Patterns collected at the edge exhibit spurious peaks at $Q \approx 0.57$ Å^{-1} (noted with the black arrow) as well as at 0.93 Å^{-1}. For comparison, the integral intensity of the (222) peak of HKUST-1 ($Q \approx 0.83$ Å^{-1}) is mapped for each slice (e,g, respectively) as well as the integral intensity of the peak at $Q \approx 0.57$ Å^{-1} (f,h, respectively). (d) PDF components derived from NMF of all total scattering mapping data; the fractional weighting of components A (i,k) and B (j,l) are mapped to depict their distribution across the monolith.

at the bulk level. To further examine the local environment, we analyzed $_{mono}$HKUST-1 by Raman microscopy. Raman spectra were initially collected by focusing on two independent regions of the monolithic sample corresponding to the lighter and darker blue sections, respectively, as seen by optical microscopy (Figures 3d and S33–S35); Figure S36 shows the Raman spectra for both sections. The dark blue regions display a spectrum that was found to be similar to previous reports on HKUST-1,[33] whereas the lighter blue region contains additional peaks that can be attributed to BTC^{3-} hydrates and copper paddlewheel hydration. When the Raman mapping was performed (Figure 3e,f), by monitoring the normalized scores obtained from classic least squares (CLS) regression analysis and fitting the full spectra obtained from the dark and light blue regions of the $_{mono}$HKUST-1 material, we can see a clear trend. Here, the spectrum associated with HKUST-1 becomes dominant as the Raman probe moves from the lighter blue to the darker blue section.

We further probed the structural heterogeneity of $_{mono}$HKUST-1 using synchrotron X-ray scattering experiments across multiple length scales by small-angle X-ray scattering (SAXS), PDF, and X-ray diffraction (XRD). We used SAXS (Figure S31) to determine the size of the primary MOF particles for both monolithic and powdered HKUST-1. Interestingly, while the $_{mono}$HKUST-1 sample contains primary particles with a spherical diameter of *ca.* 20 nm (Figure S32), the powdered HKUST-1 sample was found to contain two broader distributions, with particles of *ca.* 24 to 92 nm in diameter. To evaluate the uniformity of the monolith, we sectioned $_{mono}$HKUST-1 samples into *ca.* 1 mm segments (Figure S27) and mapped them in two dimensions with 500 μm^2 resolution (Figure 4a). Diffraction patterns revealed differences in the scattering data collected from probe volumes at the external surface of the monolith (Figure 4b,c). To compare the relative presence of impurities, the normalized integral intensity of the spurious diffraction peak at $Q = 0.83$ Å^{-1} and the (222) peak ($Q = 0.83$ Å^{-1}) of HKUST-1 was fitted using the cumulative trapezoid method as implemented in the Python package scipy.integrate (Figure 4e–h). To further probe the monolithic HKUST-1 PDF, we analyzed the data using previously described non-negative matrix factorization (NMF) techniques.[34] Two components were used to describe the data (Figures 4d,i–l and S29). Comparison of these maps (Figure S30) reveals reasonable corroboration between the PDF-NMF components and the spurious diffraction peaks observed, with component A having a mean Pearson correlation of 0.92 with the (222) peak of slice 1 and 0.98 with the (222) peak of slice 2, and component B having a mean Pearson correlation of 0.78 with the spurious peak of slice 1 and 0.91 with the spurious peak of slice 2. Diffractograms collected in this region included additional peaks consistent with those previously ascribed to the hydrolytic decomposition of HKUST-1[35] (Figure 4l). In contrast, the center of the monolith samples exhibited little to no presence of these peaks (Figure 4j) and fitted well with an HKUST-1 model without evidence of impurities. Indeed, this mapping matches with an observed difference in color between the center (dark blue) and edge (light blue) of the sample. Taking into account the above observations on Raman scattering, this further suggests the existence of HKUST-1 and a hydrated form, respectively.[33] An analysis of the PDF data decomposed the data into two phases that correlate well with the distribution of HKUST-1 and the additional diffraction peaks. The PDF component corresponding to additional diffraction peaks exhibits limited radial distance atom–atom correlations with the exception of an increase in Cu–Cu distances, consistent with the hydration of the paddlewheel (Figure S30). It is remarkable that densification of the material in $_{mono}$HKUST-1 not only improves volumetric adsorption but may also improve the hydrolytic stability of the material by limiting accessible surfaces to the outer edges of the monolith. The hydration of the Cu paddlewheels on the outer surfaces of $_{mono}$HKUST-1 may act in a "sacrificial" manner similar to that observed for STAM-17-OEt, enabling the retention of the bulk

https://doi.org/10.1021/jacs.2c04608
J. Am. Chem. Soc. 2022, 144, 13729–13739

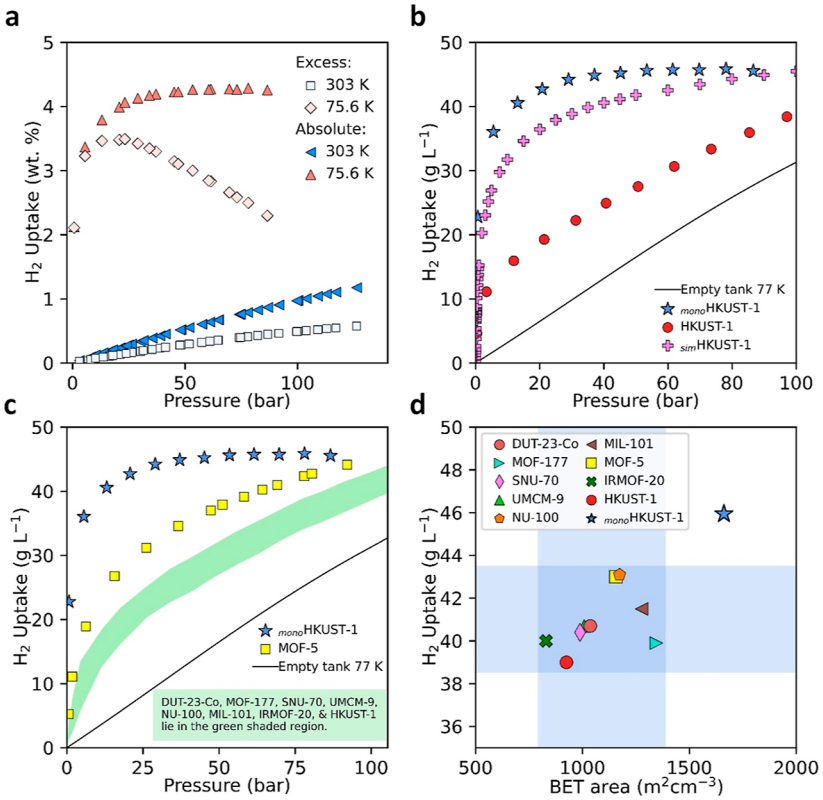

Figure 5. H_2 adsorption isotherms of densified and monolithic MOF materials. (a) Excess and total (N_{abs}) H_2 adsorption isotherms for $_{mono}$HKUST-1 measured at 75.6 K (liquid nitrogen measurement made at the National Renewable Energy Laboratory, elevation 5768 feet (1758 m)) and 303 K. An envelope density of 1.07 g mL^{-1} was used to calculate the volumetric H_2 uptake of the $_{mono}$HKUST-1 material. (b) High-pressure absolute (N_{abs}) H_2 isotherms of $_{mono}$HKUST-1 compared to pressed HKUST-1 powder and simulated HKUST-1 uptake at 77 K. (c) 77 K H_2 adsorption isotherms of $_{mono}$HKUST-1 and previously reported densified MOFs.[12,41] (d) 100 bar and 77 K H_2 adsorption capacity vs volumetric BET area of $_{mono}$HKUST-1 and previously reported benchmark densified MOF materials.[12,41]

porosity upon exposure to moisture.[36] This was confirmed using 77 K N_2 adsorption isotherms, which were performed on a $_{mono}$HKUST-1 sample stored at room temperature for 18 months. This sample was found to retain over 90% of its overall BET area and porosity after 18 months of storage (Figure S48). The monolithic nature was found to significantly improve the chemical stability of the $_{mono}$HKUST-1 material.

Hydrogen Storage Performance. To probe the improved performance of densified MOFs in H_2 storage, we collected high-pressure adsorption isotherms at eight temperatures from 75.6 to 303 K and up to 140 bar (Figures 5 and S12−S15) on $_{mono}$HKUST-1. To ensure reproducibility of the data, this was done in three separate laboratories: NREL, the University of Alicante, and the University of Cambridge. It is important to note that the experimentally measured values are excess amounts adsorbed (N_{exc}), which were then transformed into absolute uptakes (N_{abs}) by using eq 1 (Supporting Information, eq 5)

$$N_{abs} = N_{exc} + \rho V_{pore} \quad (1)$$

where ρ is the density of the gas at the given adsorption pressure and temperature, obtained from the National Institute of Standards and Technology (NIST),[37] and V_{pore} is the pore volume of the adsorbent.[27] The calculated absolute adsorption (N_{abs}) (Supporting Information, eq 5) based on excess (N_{exc}) H_2 isotherms collected at 75.6, 77, and 77 K (Figures 5a, S14, and S15) at NREL, the University of Cambridge, and the University of Alicante, respectively, were found to be in good agreement, displaying similar H_2 uptakes at corresponding pressures for each of the three isotherms. Figures S12 and S13 display the NREL excess and calculate total (N_{tot}) (Supporting Information, eq 6) H_2 uptake at 75.6 and 303 K for comparison.[38−40] Figure 5b shows the absolute (N_{abs}) volumetric adsorption isotherms of H_2 at 75.6 K in $_{mono}$-HKUST-1 compared with a densified HKUST-1 powder and a simulated H_2 isotherm for HKUST-1. The difference between isotherms is striking; interestingly, $_{mono}$HKUST-1 displays higher H_2 uptake at lower pressures compared to the densified powder sample, achieving a saturation uptake of *ca.* 46 g L^{-1} at 50 bar. In comparison, the densified HKUST-1 powder achieves an uptake of only *ca.* 28 g L^{-1} at 50 bar and of *ca.* 38 g L^{-1} at 100 bar. In comparison, the simulated absolute H_2 uptake of HKUST-1 (*ca.* 45 g L^{-1}) and $_{mono}$HKUST-1 isotherms displays similar features. The higher uptake of $_{mono}$HKUST-1 compared to the simulated isotherm can be attributed to the envelope density observed in $_{mono}$HKUST-1 (1.07 g cm^{-3}), which exceeds the theoretical crystal density for HKUST-1 (0.883 g cm^{-3}).

Figure 5c compares the volumetric H_2 adsorption performance of $_{mono}$HKUST-1 with the performance of previously reported densified MOF materials (Figure S41) using real bulk densities of the materials;[12,13,31,41−44] Figure S40 compares the performance of $_{mono}$HKUST-1 with the performance of previously reported benchmark MOF materials, with the caveat that this is done based on theoretical single-crystal density.[10,24,25,45,46] Typically, a densified polycrystalline

https://doi.org/10.1021/jacs.2c04608
J. Am. Chem. Soc. 2022, 144, 13729−13739

powder, as described above, will be many times limited to a density 50% lower than the theoretical crystal density.[12,16] Importantly, a recent report has shown that the precise control of the MOF particle's shape and size can give way to improved bulk densities in shaped MOF materials.[18] Although the gravimetric H_2 uptake of $_{mono}$HKUST-1 is lower than that of all the previously reported materials studied herein (Table S19), the $_{mono}$HKUST-1 material displays benchmark volumetric H_2 adsorption performance. The closest material to $_{mono}$HKUST-1 in terms of performance is MOF-5, displaying a H_2 adsorption capacity of *ca.* 43 g L^{-1} at 100 bar. The performance of $_{mono}$HKUST-1 was also found to outperform the benchmark carbon-based material AX21 at 100 bar and 77 K (Table S19).[47] The H_2 uptake performance of $_{mono}$HKUST-1 at 25 and 50 bar exceeds the 100 bar uptake of the densified powder MOFs (Table S19, Figures 5c and S42). The exceptional performance of the $_{mono}$HKUST-1 sample is attributed to the high bulk density achieved *via* a sol−gel synthesis approach, overcoming the lower densities and mechanical degradation issues associated with traditional powder pressing techniques.[12,16] The effects of mechanical pressing of MOFs have a detrimental impact on the overall H_2 adsorption performance for storage applications.[12,16] For conformed, pressed polycrystalline powder materials, typical H_2 excess adsorption capacities are generally retained up to a point where the density is increased up to *ca.* 50% of the single-crystal density (Figure S47). After that point, although the density continues to increase, the maximum excess adsorption value starts to decrease due to the continued mechanical collapse of the MOF.[12,16] In contrast, the $_{mono}$HKUST-1 sample was found to retain a high H_2 adsorption capacity at bulk densities exceeding those of the crystal density of HKUST-1 (i.e., 1.07 vs 0.883 g cm^{-3}). As has been seen elsewhere, the high-pressure H_2 adsorption performance of the densified MOFs was found to follow a similar trend to that of the volumetric BET areas of the materials studied (Figure 5d).[12,25] This means that volumetric BET area, using an appropriate density, is a valuable descriptor to predict the volumetric performance of MOFs.

To determine the adsorbate−adsorbent interaction energies for $_{mono}$HKUST-1, we calculated the isosteric heats of adsorption (Q_{st}) from H_2 isotherms collected at eight temperatures using the Virial method (Figures S38 and S39). The experimental Q_{st} value for $_{mono}$HKUST-1 was found to be in the range of 3.7−5.5 kJ mol^{-1}. This value was found to be consistent with previously reported values for HKUST-1 in addition to other benchmark copper paddlewheel MOFs (NOTT-112 and NU-125).[25] Q_{st} is an important variable in understanding how easy it is to release the gases at lower pressures and/or higher temperatures. Indeed, the storage and release temperatures are another key factor for H_2 storage materials. Since the current DOE targets only address hydrogen delivery temperature (−40 to 85 °C, to meet fuel cell system operation specifications) and not the storage system operating temperature, a range of possible system designs can be considered. To assess the performance of $_{mono}$HKUST-1 over a wide range of temperatures, we applied the dual-process Langmuir (DPL)[48] equation to the experimental isotherms (Figures S16−S25). We found the DPL equation to be in good agreement with the experimental data collected at eight temperatures. The initial conditions assessed for storage of H_2 were near ambient (−75 to 100 °C) up to 100 bar (Figure 6a and Table S21). $_{mono}$HKUST-1

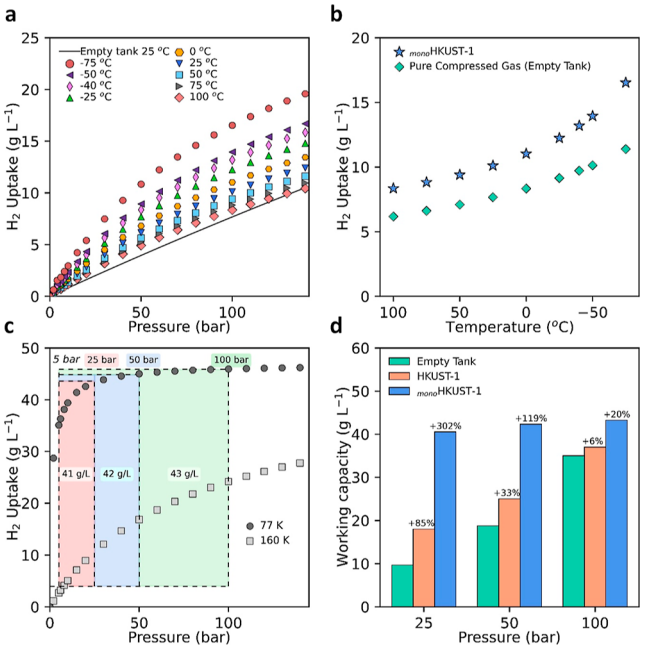

Figure 6. $_{mono}$HKUST-1 H_2 storage working capacities. (a) Near-ambient absolute H_2 adsorption isotherms for $_{mono}$HKUST-1 compared to compressed H_2 gas at 25 °C. (b) Gas storage performance at 100 bar of $_{mono}$HKUST-1 compared to compressed gas at near-ambient temperatures. (c) Cryogenic H_2 gas delivery for the temperature−pressure swing (100 bar/77 K → 5 bar/160 K) storage system. (d) Deliverable H_2 capacity of $_{mono}$HKUST-1 compared to HKUST-1 powder and an empty tank at various adsorption pressures at 77 K.

displays a H_2 adsorption capacity of 10.1 g L^{-1} at 25 °C and 100 bar, which is, to the best of our knowledge, the highest measured H_2 capacity of a densified MOF—using real MOF density—under these conditions. However, the usable capacity in this case, with no temperature swing, is slightly reduced to 9.3 g L^{-1} due to the uptake of 0.84 g L^{-1} at 5 bar. This still outperforms compressed hydrogen, which would require compression to over 150 bar to obtain the same total volumetric usable capacity at 25 °C (Figure 6b). At 100 bar and a temperature of −75 °C, $_{mono}$HKUST-1 takes up a total of 16.5 g L^{-1} H_2, which corresponds to a total usable capacity of 14.8 g L^{-1}. If the use of a temperature swing in a storage system is considered, through the application of active cooling at high filling levels, the usable capacities attained with $_{mono}$HKUST-1 are even higher. For example, adsorption at −40 °C and desorption at 25 °C afford a usable capacity of 12.4 g L^{-1}. A temperature swing from adsorption at −75 °C to desorption at 25 °C gives a usable capacity of 15.7 g L^{-1}. This usable capacity represents the highest H_2 volumetric usable capacity achieved to date for a densified adsorbent operating in this temperature range. Although these values are comparable to the current theoretical benchmarks (Ni_2(dobdc), MOF-5, and $V_2Cl_{2.8}$(btdd))[10,49] under these conditions (Table S21), it is important to highlight that these previous values are based on theoretical crystal densities and not experimental envelope densities, as reported here for $_{mono}$HKUST-1. A natural assumption is to expect a *ca.* 50% reduction in the density and therefore in volumetric capacities in densified powders.[12,16]

When cryogenic conditions are employed for H_2 storage, the use of a temperature swing step (i.e., 77 to 160 K) can increase

https://doi.org/10.1021/jacs.2c04608
J. Am. Chem. Soc. 2022, 144, 13729−13739

the usable capacities by increasing the quantity of H_2 desorbed upon cycling. While $_{mono}$HKUST-1 displays an overall H_2 uptake of 46.0 g L^{-1} at 100 bar and 77 K, the high H_2 uptake at low pressures limits the working capacity to 11.2 g L^{-1}. When a combined temperature−pressure swing system (100 bar/77 K → 5 bar/160 K) is employed, the working capacity increases to 43.3 g L^{-1} (Figure 6c). This exceeds the performance of all densified MOF benchmarks under similar conditions (Table S20).[12] Although, a priori, this may sound contrary to the results obtained from the HTS, here it is important to point out that the force fields used in simulations tend to under-predict the H_2 uptake for MOFs containing open-metal sites—including benchmark MOFs such as HKUST-1, NU-100, Ni(dobdc), and MIL-101 considered in this study—particularly at low pressures where polarization can play a significant role in H_2 adsorption.[50] Also, the structures used in silico are perfect single crystals and do not contain defects such as missing linkers, missing clusters, and so forth commonly seen in experimental structures. Combined, this can lead to differences between experimentally determined and theoretically delivered capacities. Interestingly, the $_{mono}$-HKUST-1 sample reaches >95% (43.8 g L^{-1}) saturation at 25 bar, enabling H_2 saturation at much lower pressures compared to many benchmark MOFs. When lower adsorption pressures are taken into account (Figure 6d), $_{mono}$HKUST-1 exhibits working capacities of 42.3 and 40.5 g L^{-1}, for loading pressures of 50 (50 bar/77 K → 5 bar/160 K) and 25 bar (25 bar/77 K → 5 bar/160 K), respectively. These values represent a 302 and 119% increase in the H_2 volumetric storage capacities of an empty tank at 25 and 50 bar, respectively. By comparison, under ambient temperatures, H_2 gas would need to be pressurized to 145 and 700 bar at 77 and 298 K, respectively, to achieve similar storage capacities. Again, to the best of our knowledge, this is the highest deliverable capacity achieved by any adsorbent after successful pelletization and shaping.

To design a material for adsorption applications, its volumetric capacity is not the only parameter that needs to be taken into consideration. Looking at the DOE targets, heat management due to the exo/endothermic nature of the adsorption/desorption phenomena, as well as efficient packing of a monolith in a tank, impurity tolerance (e.g., CO, H_2O), recyclability (e.g., 100 cycles), and cost of adsorbent need to be optimized. In the case of $_{mono}$HKUST-1, the three times higher density compared with that of the powder is expected to improve heat transfer significantly. Moreover, the generic approach of the sol−gel synthesis also allows for doping with materials such as activated carbon with higher thermal conductivity.[11] In terms of cost, the primary limiting factors for $_{mono}$HKUST-1 production include the starting materials' cost, high solvent usage, and centrifuge cycling times.[51−53] Solvent reduction and recovery combined can massively reduce $_{mono}$HKUST-1 production costs (Figure S50). Additionally, by employing liquid-assisted grinding, it is possible to significantly reduce mixing times by using prepared nanocrystalline powders to form high-density $_{mono}$HKUST-1 materials while maintaining monolith quality (Figure S49). Predictably, yield is also a large cost driver, and any cost-effective production will seek to maximize yield. The simplicity of the synthesis of monolithic MOFs combined with their exceptional performance indicates that monolithic MOFs could play an important role in fuel gas storage in the coming decades.

CONCLUSIONS

In conclusion, we have investigated computationally the landscape of MOFs for H_2 storage and selected HKUST-1 as the optimal structure due to its adsorption capacity and ease of synthesis. Following this, we synthesized and analyzed the structure and H_2 adsorption properties of the monolithic version, $_{mono}$HKUST-1. SAXS, NMR spectroscopy, and Raman microscopy studies demonstrated that $_{mono}$HKUST-1 exhibits similar characteristics in terms of composition and connectivity to powdered HKUST-1. However, the small and uniform primary particles result in exceptionally close packing, giving way to high-density final materials when mild drying conditions are applied. The monolithic structure of $_{mono}$-HKUST-1 also gives way to reduced material degradation, a common issue with HKUST-1 powders. The high-density structure forms an oxidized layer on the external surface which reduces the exposure of HKUST-1 particles within the monolith to moisture, maintaining exceptional performance after prolonged periods of exposure to the atmosphere. The exceptional high-density structure of $_{mono}$HKUST-1 gives way to record-breaking H_2 storage performance. The unique synthesis mechanism for $_{mono}$HKUST-1 enables the formation of materials that maintain porosity after shaping and display benchmark volumetric BET areas, which in turn gives way to exceptional H_2 sorption performance. The $_{mono}$HKUST-1 materials were found to be capable of achieving H_2 working capacities at 25 bar under cryogenic conditions, which was only possible by compressing H_2 to 700 bar at room temperature. This reduction in operating pressures has the potential to significantly reduce the systemwide engineering requirements and cost while simultaneously improving the overall safety of onboard H_2 storage for vehicular transport. While further development is required to identify more stable materials with high working capacities, this work represents a significant step forward in the shaping and densification of MOFs for H_2 storage applications.

ASSOCIATED CONTENT

Supporting Information

The Supporting Information is available free of charge at https://pubs.acs.org/doi/10.1021/jacs.2c04608.

Additional experimental procedures, in situ procedures and results, and computational information (PDF)

Full details of previous high-throughput screening (HTS) studies of MOFs for H_2 storage (XLSX)

AUTHOR INFORMATION

Corresponding Authors

David Gerard Madden − *The Adsorption & Advanced Materials Laboratory (A²ML), Department of Chemical Engineering & Biotechnology, University of Cambridge, Cambridge CB3 0AS, U.K.; Department of Chemical Sciences and Bernal Institute, University of Limerick, Limerick V94 T9PX, Ireland;* orcid.org/0000-0003-3875-9146; Email: dm850@cam.ac.uk

Karena W. Chapman − *Department of Chemistry, Stony Brook University, Stony Brook, New York 11790-3400, United States;* orcid.org/0000-0002-8725-5633; Email: karena.chapman@stonybrook.edu

David Fairen-Jimenez − *The Adsorption & Advanced Materials Laboratory (A²ML), Department of Chemical Engineering & Biotechnology, University of Cambridge,*

Cambridge CB3 0AS, U.K.; orcid.org/0000-0002-5013-1194; Email: df334@cam.ac.uk

Authors

Daniel O'Nolan − *Department of Chemistry, Stony Brook University, Stony Brook, New York 11790-3400, United States*

Nakul Rampal − *The Adsorption & Advanced Materials Laboratory (A²ML), Department of Chemical Engineering & Biotechnology, University of Cambridge, Cambridge CB3 0AS, U.K.;* orcid.org/0000-0002-6187-5631

Robin Babu − *The Adsorption & Advanced Materials Laboratory (A²ML), Department of Chemical Engineering & Biotechnology, University of Cambridge, Cambridge CB3 0AS, U.K.*

Ceren Çamur − *The Adsorption & Advanced Materials Laboratory (A²ML), Department of Chemical Engineering & Biotechnology, University of Cambridge, Cambridge CB3 0AS, U.K.*

Ali N. Al Shakhs − *The Adsorption & Advanced Materials Laboratory (A²ML), Department of Chemical Engineering & Biotechnology, University of Cambridge, Cambridge CB3 0AS, U.K.*

Shi-Yuan Zhang − *The Adsorption & Advanced Materials Laboratory (A²ML), Department of Chemical Engineering & Biotechnology, University of Cambridge, Cambridge CB3 0AS, U.K.;* orcid.org/0000-0002-7199-2938

Graham A. Rance − *Nanoscale and Microscale Research Center (nmRC), University of Nottingham, Nottingham NG7 2RD, U.K.; School of Chemistry, University of Nottingham, Nottingham NG7 2RD, U.K.;* orcid.org/0000-0002-8325-1096

Javier Perez − *Synchrotron SOLEIL, Saint-Aubin 91190, France*

Nicola Pietro Maria Casati − *10 Laboratory for Synchrotron Radiation—Condensed Matter, Paul Scherrer Institute, Villigen 5232, Switzerland;* orcid.org/0000-0002-4206-9239

Carlos Cuadrado-Collados − *Laboratorio de Materiales Avanzados (LMA), Departamento de Química Inorgánica-IUMA, Universidad de Alicante, San Vicente del Raspeig 03690, Spain*

Denis O'Sullivan − *Immaterial Ltd., Cambridge CB4 0FW, U.K.*

Nicholas P. Rice − *Immaterial Ltd., Cambridge CB4 0FW, U.K.*

Thomas Gennett − *Materials and Chemical Science and Technology Directorate, National Renewable Energy Laboratory, Golden, Colorado 80401, United States*

Philip Parilla − *Materials and Chemical Science and Technology Directorate, National Renewable Energy Laboratory, Golden, Colorado 80401, United States*

Sarah Shulda − *Materials and Chemical Science and Technology Directorate, National Renewable Energy Laboratory, Golden, Colorado 80401, United States*

Katherine E. Hurst − *Materials and Chemical Science and Technology Directorate, National Renewable Energy Laboratory, Golden, Colorado 80401, United States;* orcid.org/0000-0003-4596-9504

Vitalie Stavila − *Chemistry, Combustion, and Materials Science Center, Sandia National Laboratories, Livermore, California 94551, United States;* orcid.org/0000-0003-0981-0432

Mark D. Allendorf − *Chemistry, Combustion, and Materials Science Center, Sandia National Laboratories, Livermore, California 94551, United States;* orcid.org/0000-0001-5645-8246

Joaquin Silvestre-Albero − *Laboratorio de Materiales Avanzados (LMA), Departamento de Química Inorgánica-IUMA, Universidad de Alicante, San Vicente del Raspeig 03690, Spain;* orcid.org/0000-0002-0303-0817

Alexander C. Forse − *Yusuf Hamied Department of Chemistry, University of Cambridge, Cambridge CB2 1EW, U.K.;* orcid.org/0000-0001-9592-9821

Neil R. Champness − *School of Chemistry, University of Birmingham, Birmingham B15 2TT, U.K.;* orcid.org/0000-0003-2970-1487

Complete contact information is available at: https://pubs.acs.org/10.1021/jacs.2c04608

Author Contributions

‖‖D.G.M., D.O'N., and N.R. contributed equally.

Notes

The authors declare the following competing financial interest(s): David Fairen-Jimenez has a financial interest in the start-up company Immaterial Ltd., which is seeking to commercialize metalorganic frameworks.

■ ACKNOWLEDGMENTS

D.F.-J. thanks the European Research Council (ERC) under the European Union's Horizon 2020 research and innovation programme (NanoMOFdeli), ERC-2016-COG 726380, Innovate UK (104384), and EPSRC IAA (IAA/RG85685). D.G.M. acknowledges the SFI-IRC Pathways award (21/PATH-S/9648) from Science Foundation Ireland and the European Union's Horizon 2020 research and innovation programme under the Marie Skłodowska-Curie grant Agreement No. 801165 (Project ID: MF20210297). J.S.A. would like to acknowledge the financial support from MINECO (PID2019-108453GB-C21 and PCI2020-111968). N.R.C. thanks the Engineering and Physical Sciences Research Council, United Kingdom (EP/S002995/1), for support. This work was also supported by a UKRI Future Leaders Fellowship to A.C.F. (MR/T043024/1). M.D.A. and V.S. gratefully acknowledge research support from the U.S. Department of Energy, Office of Energy Efficiency and Renewable Energy, Fuel Cell Technologies Office through the Hydrogen Storage Materials Advanced Research Consortium (HyMARC). Sandia National Laboratories is a multimission laboratory managed and operated by the National Technology and Engineering Solutions of Sandia, LLC, a wholly owned subsidiary of Honeywell International Inc., for the U.S. Department of Energy's National Nuclear Security Administration under contract DE-NA0003525. The authors acknowledge SOLEIL for the provision of the synchrotron radiation facility and the SWING beamline for access to the instrumentation (Project no. 20200126). N.R. acknowledges the support of the Cambridge International Scholarship and the Trinity Henry Barlow Scholarship (Honorary). We also thank Prof. Omar Farha (Northwestern University) and Prof. Donald Siegel (University of Michigan) for providing .cif files for NU-1500-Al and UMCM-9, respectively.

REFERENCES

(1) Economy, H. Looking at the Hydrogen Economy. *Nature* **1973**, *243*, 184−185.
(2) Marbán, G.; Valdés-Solís, T. Towards the Hydrogen Economy? *Int. J. Hydrogen Energy* **2007**, *32*, 1625−1637.
(3) Bockris, J. O. M. A Hydrogen Economy. *Science* **1972**, *176*, 1323.
(4) U.S Deparment of Energy. DOE Technical Targets for Onboard Hydrogen Storage for Light-Duty Vehicles; Department of Energy https://www.energy.gov/eere/fuelcells/doe-technical-targets-onboard-hydrogen-storage-light-duty-vehicles%0Ahttps://energy.gov/eere/fuelcells/doe-technical-targets-onboard-hydrogen-storage-light-duty-vehicles (accessed Feb 20, 2020).
(5) Zubizarreta, L.; Arenillas, A.; Pis, J. J. Carbon Materials for H2 Storage. *Int. J. Hydrogen Energy* **2009**, *34*, 4575−4581.
(6) Kumar, K. V.; Preuss, K.; Titirici, M. M.; Rodríguez-Reinoso, F. Nanoporous Materials for the Onboard Storage of Natural Gas. *Chem. Rev.* **2017**, *117*, 1796−1825.
(7) Nazir, H.; Muthuswamy, N.; Louis, C.; Jose, S.; Prakash, J.; Buan, M. E.; Flox, C.; Chavan, S.; Shi, X.; Kauranen, P.; et al. Is the H2 Economy Realizable in the Foreseeable Future? Part II: H2 Storage, Transportation, and Distribution. *Int. J. Hydrogen Energy* **2020**, *45*, 20693−20708.
(8) Moghadam, P. Z.; Li, A.; Liu, X. W.; Bueno-Perez, R.; Wang, S. D.; Wiggin, S. B.; Wood, P. A.; Fairen-Jimenez, D. Targeted Classification of Metal-Organic Frameworks in the Cambridge Structural Database (CSD). *Chem. Sci.* **2020**, *11*, 8373−8387.
(9) Sarkisov, L.; Bueno-Perez, R.; Sutharson, M.; Fairen-Jimenez, D. Materials Informatics with PoreBlazer v4.0 and the CSD MOF Database. *Chem. Mater.* **2020**, *32*, 9849−9867.
(10) Kapelewski, M. T.; Runčevski, T.; Tarver, J. D.; Jiang, H. Z. H.; Hurst, K. E.; Parilla, P. A.; Ayala, A.; Gennett, T.; FitzGerald, S. A.; Brown, C. M.; et al. Record High Hydrogen Storage Capacity in the Metal-Organic Framework Ni2(m-Dobdc) at Near-Ambient Temperatures. *Chem. Mater.* **2018**, *30*, 8179−8189.
(11) Purewal, J.; Liu, D.; Sudik, A.; Veenstra, M.; Yang, J.; Maurer, S.; Müller, U.; Siegel, D. J. Improved Hydrogen Storage and Thermal Conductivity in High-Density MOF-5 Composites. *J. Phys. Chem. C* **2012**, *116*, 20199−20212.
(12) Purewal, J.; Veenstra, M.; Tamburello, D.; Ahmed, A.; Matzger, A. J.; Wong-Foy, A. G.; Seth, S.; Liu, Y.; Siegel, D. J. Estimation of System-Level Hydrogen Storage for Metal-Organic Frameworks with High Volumetric Storage Density. *Int. J. Hydrogen Energy* **2019**, *44*, 15135−15145.
(13) Purewal, J. J.; Liu, D.; Yang, J.; Sudik, A.; Siegel, D. J.; Maurer, S.; Müller, U. Increased Volumetric Hydrogen Uptake of MOF-5 by Powder Densification. *Int. J. Hydrogen Energy* **2012**, *37*, 2723−2727.
(14) Moghadam, P. Z.; Rogge, S. M. J.; Li, A.; Chow, C. M.; Wieme, J.; Moharrami, N.; Aragones-Anglada, M.; Conduit, G.; Gomez-Gualdron, D. A.; Van Speybroeck, V.; et al. Structure-Mechanical Stability Relations of Metal-Organic Frameworks via Machine Learning. *Matter* **2019**, *1*, 219−234.
(15) Connolly, B. M.; Madden, D. G.; Wheatley, A. E. H.; Fairen-Jimenez, D. Shaping the Future of Fuel: Monolithic Metal-Organic Frameworks for High-Density Gas Storage. *J. Am. Chem. Soc.* **2020**, *142*, 8541−8549.
(16) Peng, Y.; Krungleviciute, V.; Eryazici, I.; Hupp, J. T.; Farha, O. K.; Yildirim, T. Methane Storage in Metal-Organic Frameworks: Current Records, Surprise Findings, and Challenges. *J. Am. Chem. Soc.* **2013**, *135*, 11887−11894.
(17) Tian, T.; Zeng, Z.; Vulpe, D.; Casco, M. E.; Divitini, G.; Midgley, P. A.; Silvestre-Albero, J.; Tan, J. C.; Moghadam, P. Z.; Fairen-Jimenez, D. A Sol-Gel Monolithic Metal-Organic Framework with Enhanced Methane Uptake. *Nat. Mater.* **2018**, *17*, 174−179.
(18) Suresh, K.; Aulakh, D.; Purewal, J.; Siegel, D. J.; Veenstra, M.; Matzger, A. J. Optimizing Hydrogen Storage in MOFs through Engineering of Crystal Morphology and Control of Crystal Size. *J. Am. Chem. Soc.* **2021**, *143*, 10727−10734.
(19) Mehta, J. P.; Tian, T.; Zeng, Z.; Divitini, G.; Connolly, B. M.; Midgley, P. A.; Tan, J. C.; Fairen-Jimenez, D.; Wheatley, A. E. H. Sol−Gel Synthesis of Robust Metal−Organic Frameworks for Nanoparticle Encapsulation. *Adv. Funct. Mater.* **2018**, *28*, 1705588.
(20) Connolly, B. M.; Aragones-Anglada, M.; Gandara-Loe, J.; Danaf, N. A.; Lamb, D. C.; Mehta, J. P.; Vulpe, D.; Wuttke, S.; Silvestre-Albero, J.; Moghadam, P. Z.; et al. Tuning Porosity in Macroscopic Monolithic Metal-Organic Frameworks for Exceptional Natural Gas Storage. *Nat. Commun.* **2019**, *10*, 2345.
(21) Tian, T.; Velazquez-Garcia, J.; Bennett, T. D.; Fairen-Jimenez, D. Mechanically and Chemically Robust ZIF-8 Monoliths with High Volumetric Adsorption Capacity. *J. Mater. Chem. A* **2015**, *3*, 2999−3005.
(22) Moghadam, P. Z.; Li, A.; Wiggin, S. B.; Tao, A.; Maloney, A. G. P.; Wood, P. A.; Ward, S. C.; Fairen-Jimenez, D. Development of a Cambridge Structural Database Subset: A Collection of Metal-Organic Frameworks for Past, Present, and Future. *Chem. Mater.* **2017**, *29*, 2618−2625.
(23) Ahmed, A.; Seth, S.; Purewal, J.; Wong-Foy, A. G.; Veenstra, M.; Matzger, A. J.; Siegel, D. J. Exceptional Hydrogen Storage Achieved by Screening Nearly Half a Million Metal-Organic Frameworks. *Nat. Commun.* **2019**, *10*, 1568.
(24) Chen, Z.; Li, P.; Anderson, R.; Wang, X.; Zhang, X.; Robison, L.; Redfern, L. R.; Moribe, S.; Islamoglu, T.; Gómez-Gualdrón, D. A.; et al. Balancing Volumetric and Gravimetric Uptake in Highly Porous Materials for Clean Energy. *Science* **2020**, *368*, 297−303.
(25) García-Holley, P.; Schweitzer, B.; Islamoglu, T.; Liu, Y.; Lin, L.; Rodriguez, S.; Weston, M. H.; Hupp, J. T.; Gómez-Gualdrón, D. A.; Yildirim, T.; et al. Benchmark Study of Hydrogen Storage in Metal-Organic Frameworks under Temperature and Pressure Swing Conditions. *ACS Energy Lett.* **2018**, *3*, 748−754.
(26) Barnett, B. R.; Evans, H. A.; Su, G. M.; Jiang, H. Z. H.; Chakraborty, R.; Banyeretse, D.; Hartman, T. J.; Martinez, M. B.; Trump, B. A.; Tarver, J. D.; et al. Observation of an Intermediate to H2Binding in a Metal-Organic Framework. *J. Am. Chem. Soc.* **2021**, *143*, 14884−14894.
(27) Fairen-Jimenez, D.; Colón, Y. J.; Farha, O. K.; Bae, Y. S.; Hupp, J. T.; Snurr, R. Q. Understanding Excess Uptake Maxima for Hydrogen Adsorption Isotherms in Frameworks with Rht Topology. *Chem. Commun.* **2012**, *48*, 10496−10498.
(28) Carné-Sánchez, A.; Imaz, I.; Cano-Sarabia, M.; Maspoch, D. A Spray-Drying Strategy for Synthesis of Nanoscale Metal-Organic Frameworks and Their Assembly into Hollow Superstructures. *Nat. Chem.* **2013**, *5*, 203−211.
(29) James, S. L.; Adams, C. J.; Bolm, C.; Braga, D.; Collier, P.; Friščić, T.; Grepioni, F.; Harris, K. D. M.; Hyett, G.; Jones, W.; et al. Playing with Organic Radicals as Building Blocks for Functional Molecular Materials. *Chem. Soc. Rev.* **2012**, *41*, 413−447.
(30) Osterrieth, J. W. M.; Rampersad, J.; Madden, D.; Rampal, N.; Skoric, L.; Connolly, B.; Allendorf, M. D.; Stavila, V.; Snider, J. L.; Ameloot, R.; et al. How Reproducible Are Surface Areas Calculated from the BET Equation? *Adv. Mater.* **2022**, *34*, 2201502.
(31) Allendorf, M. D.; Hulvey, Z.; Gennett, T.; Ahmed, A.; Autrey, T.; Camp, J.; Seon Cho, E.; Furukawa, H.; Haranczyk, M.; Head-Gordon, M.; et al. An Assessment of Strategies for the Development of Solid-State Adsorbents for Vehicular Hydrogen Storage. *Energy Environ. Sci.* **2018**, *11*, 2784−2812.
(32) Dawson, D. M.; Jamieson, L. E.; Mohideen, M. I. H.; McKinlay, A. C.; Smellie, I. A.; Cadou, R.; Keddie, N. S.; Morris, R. E.; Ashbrook, S. E. High-Resolution Solid-State 13C NMR Spectroscopy of the Paramagnetic Metal-Organic Frameworks, STAM-1 and HKUST-1. *Phys. Chem. Chem. Phys.* **2013**, *15*, 919−929.
(33) Prestipino, C.; Regli, L.; Vitillo, J. G.; Bonino, F.; Damin, A.; Lamberti, C.; Zecchina, A.; Solari, P. L.; Kongshaug, K. O.; Bordiga, S. Local Structure of Framework Cu(II) in HKUST-1 Metallorganic Framework: Spectroscopic Characterization upon Activation and Interaction with Adsorbates. *Chem. Mater.* **2006**, *18*, 1337−1346.
(34) O'Nolan, D.; Huang, G.; Kamm, G. E.; Grenier, A.; Liu, C. H.; Todd, P. K.; Wustrow, A.; Thinh Tran, G. T.; Montiel, D.; Neilson, J. R.; et al. A Thermal-Gradient Approach to Variabletemperature

https://doi.org/10.1021/jacs.2c04608
J. Am. Chem. Soc. 2022, 144, 13729−13739

Measurements Resolved in Space. *J. Appl. Crystallogr.* **2020**, *53*, 662−670.
(35) Terracina, A.; McHugh, L. N.; Todaro, M.; Agnello, S.; Wheatley, P. S.; Gelardi, F. M.; Morris, R. E.; Buscarino, G. Multitechnique Analysis of the Hydration in Three Different Copper Paddle-Wheel Metal-Organic Frameworks. *J. Phys. Chem. C* **2019**, *123*, 28219−28232.
(36) McHugh, L. N.; McPherson, M. J.; McCormick, L. J.; Morris, S. A.; Wheatley, P. S.; Teat, S. J.; McKay, D.; Dawson, D. M.; Sansome, C. E. F.; Ashbrook, S. E.; et al. Hydrolytic Stability in Hemilabile Metal−Organic Frameworks. *Nat. Chem.* **2018**, *10*, 1096−1102.
(37) Lemmon, E. W.; McLinden, M. O.; Friend, D. G. *Thermophysical Properties of Fluid Systems. NIST Chemistry WebBook, NIST Standard Reference Database Number 69*; National Institute of Standards and Technology: Gaithersburg MD. 2005; p 20899.
(38) Parilla, P. A.; Gross, K.; Hurst, K.; Gennett, T. Recommended Volumetric Capacity Definitions and Protocols for Accurate, Standardized and Unambiguous Metrics for Hydrogen Storage Materials. *Appl.Phys.A: Mater.Sci.Process.* **2016**, *122*, 1−18.
(39) Hurst, K. E.; Parilla, P. A.; O'Neill, K. J.; Gennett, T. An International Multi-Laboratory Investigation of Carbon-Based Hydrogen Sorbent Materials. *Appl.Phys.A: Mater.Sci.Process.* **2016**, *122*, 42.
(40) Hurst, K. E.; Gennett, T.; Adams, J.; Allendorf, M. D.; Balderas-Xicohténcatl, R.; Bielewski, M.; Edwards, B.; Espinal, L.; Fultz, B.; Hirscher, M.; et al. An International Laboratory Comparison Study of Volumetric and Gravimetric Hydrogen Adsorption Measurements. *ChemPhysChem* **2019**, *20*, 1997−2009.
(41) Ardelean, O.; Blanita, G.; Borodi, G.; Lazar, M. D.; Misan, I.; Coldea, I.; Lupu, D. Volumetric Hydrogen Adsorption Capacity of Densified MIL-101 Monoliths. *Int. J. Hydrogen Energy* **2013**, *38*, 7046−7055.
(42) Zacharia, R.; Cossement, D.; Lafi, L.; Chahine, R. Volumetric Hydrogen Sorption Capacity of Monoliths Prepared by Mechanical Densification of MOF-177. *J. Mater. Chem.* **2010**, *20*, 2145−2151.
(43) Dailly, A.; Poirier, E. Evaluation of an Industrial Pilot Scale Densified MOF-177 Adsorbent as an on-Board Hydrogen Storage Medium. *Energy Environ. Sci.* **2011**, *4*, 3527−3534.
(44) Blanita, G.; Coldea, I.; Misan, I.; Lupu, D. Hydrogen Cryo-Adsorption by Hexagonal Prism Monoliths of MIL-101. *Int. J. Hydrogen Energy* **2014**, *39*, 17040−17046.
(45) Farha, O. K.; Özgür Yazaydın, A. Ö.; Eryazici, I.; Malliakas, C. D.; Hauser, B. G.; Kanatzidis, M. G.; Nguyen, S. T.; Snurr, R. Q.; Hupp, J. T. De Novo Synthesis of a Metal-Organic Framework Material Featuring Ultrahigh Surface Area and Gas Storage Capacities. *Nat. Chem.* **2010**, *2*, 944−948.
(46) Gómez-Gualdrón, D. A.; Wang, T. C.; García-Holley, P.; Sawelewa, R. M.; Argueta, E.; Snurr, R. Q.; Hupp, J. T.; Yildirim, T.; Farha, O. K. Understanding Volumetric and Gravimetric Hydrogen Adsorption Trade-off in Metal-Organic Frameworks. *ACS Appl. Mater. Interfaces* **2017**, *9*, 33419−33428.
(47) Tian, M.; Rochat, S.; Polak-Kraśna, K.; Holyfield, L. T.; Burrows, A. D.; Bowen, C. R.; Mays, T. J. Nanoporous Polymer-Based Composites for Enhanced Hydrogen Storage. *Adsorption* **2019**, *25*, 889−901.
(48) Ritter, J. A.; Bhadra, S. J.; Ebner, A. D. On the Use of the Dual-Process Langmuir Model for Correlating Unary Equilibria and Predicting Mixed-Gas Adsorption Equilibria. *Langmuir* **2011**, *27*, 4700−4712.
(49) Jaramillo, D. E.; Jiang, H. Z. H.; Evans, H. A.; Chakraborty, R.; Furukawa, H.; Brown, C. M.; Head-Gordon, M.; Long, J. R. Ambient-Temperature Hydrogen Storage via Vanadium(II)-Dihydrogen Complexation in a Metal-Organic Framework. *J. Am. Chem. Soc.* **2021**, *143*, 6248−6256.
(50) Suepaul, S.; Forrest, K. A.; Pham, T.; Space, B. Investigating the Effects of Linker Extension on H2 Sorption in the Rht-Metal-Organic Framework NU-111 by Molecular Simulations. *Cryst. Growth Des.* **2018**, *18*, 7599−7610.
(51) Anastasopoulou, A.; Furukawa, H.; Barnett, B. R.; Jiang, H. Z. H.; Long, J. R.; Breunig, H. M. Technoeconomic Analysis of Metal-Organic Frameworks for Bulk Hydrogen Transportation. *Energy Environ. Sci.* **2021**, *14*, 1083−1094.
(52) DeSantis, D.; Mason, J. A.; James, B. D.; Houchins, C.; Long, J. R.; Veenstra, M. Techno-Economic Analysis of Metal-Organic Frameworks for Hydrogen and Natural Gas Storage. *Energy Fuels* **2017**, *31*, 2024−2032.
(53) Gaab, M.; Trukhan, N.; Maurer, S.; Gummaraju, R.; Müller, U. The Progression of Al-Based Metal-Organic Frameworks - From Academic Research to Industrial Production and Applications. *Microporous Mesoporous Mater.* **2012**, *157*, 131−136.

https://doi.org/10.1021/jacs.2c04608
J. Am. Chem. Soc. 2022, 144, 13729−13739